Morphology and Properties of Polyester/Exfoliated Graphite Nanocomposites

Hyunwoo Kim and Christopher W. Macosko*

Department of Chemical Engineering and Materials Science, University of Minnesota, Minneapolis, Minnesota 55455-0331

Received October 27, 2007; Revised Manuscript Received February 11, 2008

ABSTRACT: Nanocomposites reinforced with graphite platelets were compared to those with functionalized graphite sheets (FGS) prepared by partial pyrolysis of graphite oxide. Melt dispersion in poly(ethylene-2,6-naphthalate) (PEN) was quantified using a range of characterization techniques: electron microscopy, X-ray scattering, melt rheology, electrical conductivity, gas barrier, and mechanical properties. Conductivity percolation was obtained with as little as 0.3 vol % FGS, whereas 3 vol % was required for graphite. The threshold concentrations of FGS and graphite for rigidity percolation determined with melt rheology were in good agreement with conductivity percolation. Hydrogen permeability of PEN with 4 wt % FGS was decreased by 60% while the same amount of graphite reduced permeability only 25%. Structural differences between graphite and FGS were characterized with atomic force microscopy (AFM), Raman spectroscopy, and X-ray photoelectron spectroscopy (XPS). The highly exfoliated morphology of FGS was maintained in the composites as revealed by electron microscopy and X-ray scattering while graphite layers remained stacked together even after melt processing. Even though the tensile stiffness and dimensional stability of PEN were improved, the extent of reinforcement with FGS for these two properties was not as significant. This was attributed to the wrinkled structure of FGS and atomistic defects.

1. Introduction

Graphite is a 2-dimensional carbon material which is naturally abundant. In graphite, sp^2-hybridized carbons are covalently bonded in hexagonal manner, forming individual graphene sheets, and these sheets are bound together by van der Waals forces. Graphite has been used in many industrial applications such as lubricants[1] and high-temperature gaskets.[2] It has received attention lately due to its superior in-plane properties.[3,4] It competes with carbon nanotubes in many aspects. Its in-plane stiffness is as high as that of carbon nanotubes ($E \sim 1$ TPa),[4–6] and its electrical ($\sigma \sim 10^6$ (ohm cm)$^{-1}$)[7–9] and thermal conductivity (~400 W m^{-1} K^{-1})[10] are also exceptional. The potentially high aspect ratio of single graphene sheets indicates that graphene can greatly improve mechanical and gas barrier properties if it is well dispersed in a polymer matrix.[11,12]

However, to date, the exfoliation of graphite to graphene and its incorporation into polymers has not been successful. Because of strong interaction and small spacing between planes, it is very hard to achieve a fully separated state of graphene. Many have attempted to exfoliate graphite sheets using intercalation with alkali metals[13] or exposing them to strong acidic conditions.[14–18] Expansion of layer spacing takes place via heat treatment[13,15,17] or alternatively exposure to microwave radiation followed by mechanical grinding.[19,20] These expanded graphite platelets have been incorporated into polymer via solvent mixing,[16,21] in-situ polymerization,[17,18] or coating onto polymer particles followed by melt processing.[20] Using solvent blending, expanded graphite yielded relatively better dispersion than unintercalated graphite. However, this approach required use of expensive intercalates and solvents. Moreover, complete exfoliation to the level of single atomic sheets was not attained. A more economical approach is melt dispersion. Nanoscale reinforcements such as natural clays with surface modification have been successfully imbedded into polar polymers in the melt state by applying high shear stress using conventional melt extruders.[22,23] Although there have been approaches to employ this technique for graphite dispersion,[24,25] melt compounding has yet to yield greater enhancement in properties than solution mixing. Shen and co-workers reported that conductivity percolation can be obtained at lower filler concentration of expanded graphite via solvent intercalation than melt blending.[21] Increased stresses from intensive mixing are not enough to overcome diffusion and thermodynamic barriers originating from the extremely small interlayer spacing of graphite and incompatibility between graphite and polymer.

One way to obtain exfoliation of graphite is to use graphite that has been expanded and exfoliated prior to extrusion. It has been reported recently that highly exfoliated, functionalized graphite sheets (FGS) were produced by oxidizing graphite and conducting a rapid thermal treatment to expand interlayer spacing of graphite oxide.[26,27] Schniepp et al. reported that graphite oxide layers can be separated permanently by heating up to 1050 °C at a rate of 2000 °C/min in an argon atmosphere.[26] As a result of the thermal expansion, the surface area of graphite is enhanced significantly. However, the resulting structure of the exfoliated graphite is different from that of natural graphite.[28] The superheating process removes surface oxide groups such as CO_2, leaving atomistic defects on the surface and distorting flat graphene sheets into a highly wrinkled structure. Despite the disruption of conjugated π network of graphene by oxygen functionalization, electrical conductivity of FGS still compares with that of graphite.[26]

After incorporation of graphite into polymer, the state of dispersion must be determined adequately to evaluate the reinforcement efficiency. Among various methods used for characterizing dispersion of layered nanocomposites, electron microscopy and X-ray diffraction have been most widely used.[29,30] Imaging with transmission electron microscopy (TEM) provides real space morphological information.[23,30,31] However, TEM only visualizes a small area. On the other hand, X-ray scattering yields structural information averaged over a larger sample volume. One of the drawbacks with X-ray scattering is that it is often difficult to interpret results on the basis of reciprocal space to find out the structure and shape of the

* Corresponding author: Tel +1 612-625-0092; fax 612-626-1686; e-mail macosko@umn.edu.

10.1021/ma702385h CCC: $40.75
Published on Web 04/10/2008

scattering particles. Moreover, some minor morphological information can be missed (e.g., small amount of intercalated structure surrounded by exfoliated morphology in the case of polymer layered nanocomposites) since scattering intensity depends on the concentration of the scattering entity.

Although indirect, solid-state composite properties can be used to estimate reinforcement efficiency. These measurements are also very valuable to assess the practical performance of these composites. Composite theories for stiffness, thermal expansion, and gas barrier properties have been proposed,[32–35] and fitting experimentally measured properties with these models has provided a quantitative measure for layered composite dispersion.[36–39] However, aspect ratio data from composite theories will only be a rough estimate for dispersion since theories are based on simplified assumptions such as perfect adhesion between two phases and unidirectional alignment of disks, which are seldom realized in practice.[36] Additionally, composite modeling also requires accurate material parameters of the matrix and the reinforcement for quantitative analysis.

A polymer melt filled with nanoinclusions has distinctive rheological behavior: development of a yield stress and a frequency-independent modulus.[40–42] One can extract quantitative measures for the dispersion such as an average aspect ratio of additives from the concentration where the rigid platelets form a network having nonzero rigidity.[42–44] The threshold for this rigidity percolation can also be compared with the onset of connectivity percolation, which is easily determined from electrical conductivity measurements on nanocomposites with conducting fillers.[45,46] If there are strong colloidal interaction between platelets in the polymer matrix, then they will form fractal aggregates of reinforcing flocs.[44] With this idea, a fractal dimension of the gelled network can be inferred from how the elastic modulus and limits of linear viscoelasticity scale with the filler concentration.[47]

In this study, dispersion of unexfoliated graphite and FGS into polymer is explored with melt blending. For the matrix polymer, poly(ethylene-2,6-naphthalate), PEN, was chosen. PEN is a high-performance engineering thermoplastic which is used for many practical applications, especially in a film form for producing magnetic data storage devices.[48] The polymer substrates used for magnetic tapes must be mechanically robust and dimensionally stable upon temperature or humidity changes to enable high-density data storage. Reinforcement with nanosize inclusions will lead to better dimensional stability. We first attempted to use organically modified montmorillonite (Cloisite 20A and 30B, Southern Clay Products) as reinforcements for PEN. However, the resulting nanocomposites had high brittleness, even lower melt viscosity than neat polymer, and nearly no increase in tensile modulus. The high processing temperature, 300 °C, most likely caused thermal degradation of alkylammonium modifiers of clays. Loss of the modifiers may have resulted in poor dispersion and degradation of PEN. We then turned to graphite, which can be exfoliated without surfactants. Furthermore, its stiffness exceeds that of other inorganic nanoparticles, and its in-plane coefficient of thermal expansion is negative near room temperature.[49,50] As well as these advantages, gas permeabilities of PEN are expected to drop significantly after incorporation of graphite due to its high aspect ratio and impermeability.[12] The ability of graphite to make PEN electrically conductive is also a potential advantage for recording tapes.

In this paper, structural differences between graphite and FGS were characterized with atomic force microscopy (AFM), Raman spectroscopy, and X-ray photoelectron spectroscopy (XPS). The dispersion of graphite and FGS is examined via TEM, X-ray scattering, and melt rheology. Dispersion level from rheological measurements on molten samples is compared with results from electrical conductivity experiments as well as tensile modulus, thermal expansion, and hydrogen permeability measurements on the solid samples.

2. Experimental Section

2.1. Material Characterization. Matrix polymer, poly(ethylene-2,6-naphthalate) or PEN (X-10 PEN homopolymer, intrinsic viscosity 0.79 dL/g, *o*-chlorophenol), was obtained from Excell LLC (Dupont Polyester) in pellet form. PEN resin was dried in an oven at 120 °C for more than 24 h before melt blending. Flake graphite (surfaced enhanced, grade no. 3775) was purchased from Asbury Carbons.[51] The nominal size of particles reported by the manufacturer[1] is 8 μm, and specific surface area from BET isotherm is around 24 m^2/g. FGS, a thermally exfoliated graphite oxide with 700−1500 m^2/g of BET surface area,[26] was received from Princeton University and Vorbeck Materials.[52] The density of graphite, 2.28 g/cm^3, was calculated from unit cell dimension data of perfectly crystalline graphite (hexagonal, $a = 2.46$ and $c = 6.69$ Å),[5] and the density of FGS was assumed to be equal to that of graphite. The density of amorphous PEN (1.33 g/cm^3)[53] was used rather than density of the crystalline form (1.41−1.44 g/cm^3)[54,55] since all specimens used for the testing are highly amorphous (% crystal <5%) due to the rapid quenching after melt processing. The melt density of PEN was approximated by 1.20 g/cm^3, 90% of its amorphous density. Poly(ethylene terephthalate), which has a similar molecular structure and amorphous density (1.34 g/cm^3),[56] has the melt density of 1.20 g/cm^3.[57]

Dimensions of graphite and FGS particles as received were investigated with AFM (Proximal Nanoprobe Scanning Probe Nanoscope, Digital Instruments). Suspensions of graphite and FGS were prepared in tetrahydrofuran (THF) at 10 μg/mL by mild stirring for 72 h and deposited onto a mica substrate (grade V1, Ted Pella). Sonication was avoided since it may cause a size reduction of particles. Contact mode imaging was conducted with V-shaped gold-coated silicon nitride cantilevers (spring constant, $k = 0.12$ N/m, tip radius, $r = 20$ nm, Veeco Probes) under ambient conditions.

Raman spectroscopy and XPS were employed to probe chemical and structural differences of FGS and graphite. The Raman spectra of graphite and FGS as received were obtained using a Witec Alpha300R confocal Raman microscope connected with a class III argon laser source (Omnichrome, CA) with wavelength of 514.5 nm. For each spectrum, the signal integrated over 20 s was recorded.

X-ray photoelectron spectra of FGS powders were collected with a Physical Electronic model 555 spectrometer with Mg Kα radiation. After degassing in an introduction chamber (~1 h), samples were placed into a hemispherical analyzer where the pressure is maintained below 1.5×10^{-7} Torr. Accelerating voltage of 12 kV at 250 W power was used for data acquisition. For a single survey scan, three sweeps were averaged with pass energy of 200 eV. After identifying reflections corresponding to binding energies of C_{1s} and O_{1s}, higher resolution spectra were recorded with pass energy of 25 eV. Atomic concentration estimation and peak fitting were conducted with Auger Scan Version 3.1 program.

2.2. Melt Compounding. Before preparing blends, the PEN pellets were cryogenically pulverized to ~100 μm powders for 1 min using a Spex 6700 Freezer/Mill to prepare a more homogeneous preblend with graphite or FGS and to facilitate feeding into the extruder. PEN/graphite and PEN/FGS mixtures of 4.1−4.3 g were prepared at various graphite (0, 1, 3, 5, 6, 7, 10, 15, and 20 wt %) and FGS loadings (0.5, 1, 1.5, 2, 3, and 4 wt %). They were fed into a recirculating, conical twin-screw extruder (Microcompounder, DACA Instruments) at 280 °C with N_2 purge. Compounding was performed at a screw speed of 360 rpm for 8 min.

2.3. Direct Characterization of Dispersion. We used TEM and X-ray scattering to investigate the dispersion of graphite and FGS. DACA extruded graphite composites were microtomed into 60−90 nm thick slices at room temperature with a diamond knife (Reichert Ultracut), and digital images were obtained using a JEOL 1210 electron microscope at an accelerating voltage of 120 kV. No

straining was required to obtain good electron contrast between PEN and graphite.

X-ray scattering analysis was performed with a combined small- and wide-angle instrument (SAXSESS, Anton Paar) with Cu Kα radiation. Powders of the nanocomposite samples were produced by cryo-pulverization for 30 s and placed between Kapton tapes. A generator voltage of 40 kV and current of 50 mA were used.

2.4. Melt Rheology. Rheological measurements were carried out with a strain-controlled rotational rheometer (ARES, TA Instruments) at 290 °C under a N_2 atmosphere. 0.6−0.7 g of extruded composites was dried at 120 °C for a least 24 h and loaded onto a 25 mm parallel plate fixture. They were squeezed into disks ∼1 mm thick by slowly lowering the upper plate. After sample loading, a dynamic time sweep was conducted at 1 rad/s using small-amplitude strain until no change in storage modulus G' was observed (∼1 h). Subsequently, using a dynamic strain sweep at 1 rad/s, the critical strain, γ_{crit}, where G' drops to 90% of its limiting low strain value was recorded. After a waiting time of 30 min, a frequency sweep at $\gamma < \gamma_{crit}$ from 100 to 0.01 rad/s was started. Occasionally, an additional test from low (0.01 rad/s) to high (100 rad/s) frequency was carried out to check the long-term melt stability. Results from two consecutive frequency sweep tests were reproducible to within 10%, indicating that PEN was stable for >3 h at 290 °C.

2.5. Property Measurements. For electrical conductivity measurements, specimens with three different geometries were used to investigate the influence of processing history on electrical conductivity of composites. D samples are ∼1 mm thick disks recovered after rheology tests with long annealing history. They were removed from the rheometer plates gently to minimize deformation of samples then remelted at 300 °C and compressed slightly to make the disk surface flat. F samples are ∼70 μm thick films with a higher degree of graphite alignments. They were formed by pressing extrudates against Teflon sheets at 280 kPa and 280 °C. They were quenched into ice–water to minimize PEN crystallinity buildup after pressing and dried for at least 48 h at room temperature in a vacuum oven before property measurements. B samples are bar-shaped samples (2 cm × 3 cm × 1 mm) designed to have less graphite orientation. Extrudates were processed into powders by cryo-pulverization, and these composite powders were pressed (∼70 kPa for 10 min) and then annealed (without pressure for 1 h) in a mold at 300 °C in order to relax any preferred orientation of the graphite and FGS. After annealing, these bars were cooled in air. By differential scanning calorimetry, the D and F samples have <5% crystallinity, while the degree of crystallinity of B samples is generally around 10%. Surfaces of all the samples were polished with fine sandpaper (Wetordry Ultrafine P600) to reduce contact resistance between the sample and the conductivity probes. Surface resistance was measured with an 11-point dc probe (PRS-801 Prostat).

For the gas permeability and stiffness testing, films (F samples) were used due to their high in-plane filler orientation and small thickness. Hydrogen permeability of composite films at 35 °C was determined based on a constant volume-variable pressure method using a homemade apparatus.[58,59] Hydrogen flowing at 1 atm and 80 cm^3/min was fed to one side of a 4.2 cm diameter film sample, and the pressure in the opposite, evacuated chamber was monitored. Permeation constants were calculated using the pressure gradient, the pressure change with time, and the film thickness.[58]

Specimen for tensile modulus and thermal expansion measurements were prepared by cutting strips 4 mm wide and 30 mm long from the center of the films. They were clamped with film fixtures on a Rheometrics Solids Analyzer II. Complex moduli, E^*, were measured in dynamic strain sweep mode under 10 N static force pretension at room temperature. Thermal expansion was measured from the change in length of the same films at constant tension (∼0.1 MPa) while decreasing temperature from 65 to 45, 35, and 25 °C in a convection chamber with a dry N_2 purge. In order to exclude any effects from a hygroscopic expansion of PEN, samples were dehydrated at 65 °C for 2 h.

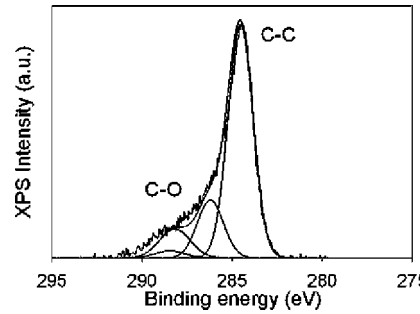

Figure 1. C_1 XPS spectrum of FGS. Peaks inside show deconvolution of the spectrum after curve fitting.

3. Results and Discussion

Graphite and FGS were characterized using contact mode AFM, Raman spectroscopy, and XPS before dispersion. After melt compounding into PEN, the state of dispersion was analyzed by TEM, X-ray scattering, and melt rheology. Then conductivity, permeability, and mechanical properties of these composites are reported.

3.1. Characterization of Graphite and FGS. Lateral and thickness dimensions of as-received graphite and FGS were analyzed using AFM. The thickness, h, of graphite averaged over 62 unaggregated particles was 37 nm. This agrees with a value of ∼30 nm calculated from the reported BET isotherm and density of graphite, assuming disk-shaped particles.[60] The AFM measured diameter of graphite ranged from 100 to 1000 nm while FGS was 50−400 nm. For FGS, thickness varied even within a single platelet due to its wrinkled and buckled nature.[26] The minimum thickness of 1.8 nm falls within the thickness range of fully exfoliated FGS found by Schniepp et al. The BET values give $h \leq 1$ nm. Reportedly,[26] the starting graphite material for FGS has a mean diameter of 45 μm. However, it is obvious that a significant reduction in diameter could occur after oxidation and pyrolysis of the graphite. Schniepp et al. also reported that the lateral size of FGS is hundreds of nanometers, in agreement with our AFM results.

Our Raman spectra of graphite and FGS powders are essentially identical to the results of Kudin et al.[61] A reflection (G band) at 1550−1650 cm^{-1} is common for both graphitic materials, which is associated with vibrations of sp^2-hybridized carbons.[62] Another reflection (D band) at 1350 cm^{-1} is prominent especially for FGS, and this vibrational mode is known to be induced by defects in sp^2 domains. The relatively higher intensity of D band and broadening of G band for FGS implies a significant transformation of sp^2 domain to sp^3 hybridization during oxidation treatments[61] and corroborates the structural distortion and weakening of the planar geometry.

The existence of oxygen functionalities on the graphene surface was confirmed by XPS. An asymmetric C_{1s} peak centered at 284.5 eV in the XPS spectrum of FGS (Figure 1) has a shoulder toward higher binding energy, which can be deconvoluted into several other peaks. Chemical shifts to the higher energy indicate the presence of other types of noncarbon bonds (C−O or C−O−C) in the aromatic domain.[26,63] These types of surface oxygen groups are expected to promote the dispersion since it will render graphene surfaces to have more polar character. The intensity at the O_{1s} level of binding energy (533 eV, not shown here) also reveals oxygen moieties on the FGS surface, from which the atomic ratio (C/O) in FGS was determined to be ∼4:1. However, the actual ratio of C to O is likely higher, up to 10:1, since XPS only measures the composition on the sample surface which can be influenced by moisture absorption.[26]

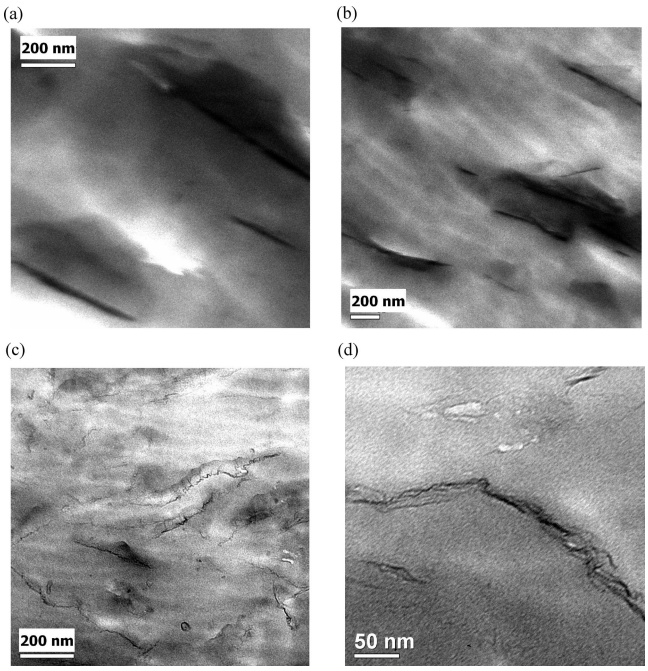

Figure 2. TEM micrographs of PEN with (a) and (b) 3 wt % graphite and (c) and (d) 3 wt % FGS.

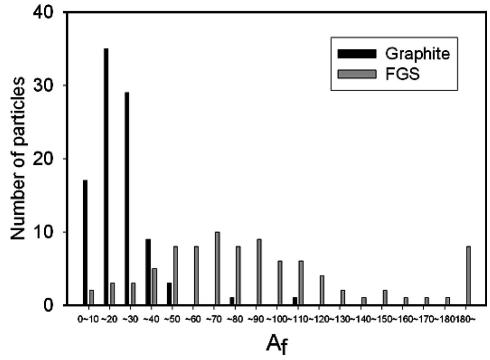

Figure 3. Shape distribution of graphite and FGS particles from TEM analysis.

3.2. TEM Analysis. TEM micrographs of PEN composites as extruded containing 3 wt % of graphite and FGS are shown in Figure 2. The graphite platelets appear as thick flat objects in Figure 2a,b. Particle dimensions were determined using an imaging analysis program. Particle thickness was defined by a full width at half-maximum (fwhm) of a line intensity profile across the particle. After investigating 95 particles, an arithmetic average of diameter and thickness of graphite are found to be 487 and 36 nm, respectively. A mean thickness of 36 nm suggests that there was no change in thickness during melt compounding when compared with the mean thickness of as-received material (37 nm) estimated by AFM. This is much greater than the interlamellar spacing of 0.34 nm, indicating each stack is composed of ~100 single graphene layers. Although melt compounding may break up weakly aggregated graphite flakes, the multiple layer structure suggests that the layers were not delaminated at all by thermodynamic interaction with PEN or by intensive shear mixing. This is probably due to strong van der Waals binding between the closely spaced graphene layers. Aspect ratios, A_f, which is the ratio of the lateral dimension to the thickness, were estimated for individual platelets, and Figure 3 shows a relatively narrow shape distribution of graphite. Its mean value is 20.8, median 18.4, and standard deviation 14.1. Interestingly, most graphite flakes

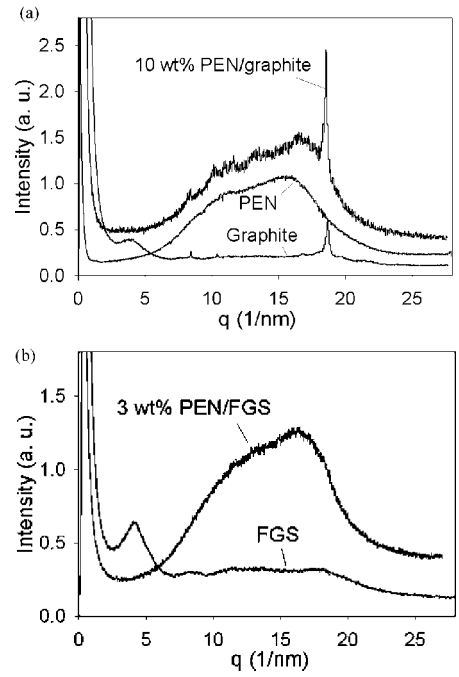

Figure 4. X-ray scattering intensity profiles of (a) graphite, PEN, and PEN/graphite composite (10 wt %) and (b) FGS and PEN/FGS composite (3 wt %).

appeared to exhibit a preferred orientation, implying alignment during extrusion process (Figure 2b).

In stark contrast with PEN/graphite, in PEN/FGS composites thin FGS sheets with high aspect ratio are distributed over the entire imaging area (Figure 2c). Statistical analysis conducted for 88 FGS particles yielded a mean diameter and thickness of 222 and 2.9 nm, respectively. Even though FGS has smaller diameter than graphite, its average aspect ratio (88.4) is greater than that of graphite (20.8) due to even smaller thickness. FGS displays a wider aspect ratio distribution than graphite as evidenced by a higher standard deviation (56.4), and an average of aspect ratio of FGS is 88.4. However, the mean aspect ratio is expected to be greater than this value since atomically thin FGS layers are likely to be invisible in TEM. Figure 2d shows the wrinkled nature of FGS which may be explained by the transformation of carbons from planar (sp^2-hybridized) to distorted structure (sp^3-hybridized) during the oxidation and pyrolysis process. This type of conversion was also confirmed by the higher D to G intensity ratio of FGS in Raman spectroscopy and the XPS results (Figure 1). There is also stacking of wrinkled sheets that resembles the so-called intercalated morphology in the nanocomposite literature. Incomplete oxide intercalation and thermal exfoliation may lead to the stacking of layers.

3.3. X-ray Scattering. Figure 4a presents X-ray scattering intensity profiles of pristine graphite, PEN, and PEN/graphite composite (10 wt %). A sharp peak located at scattering vector $q = 18.6\ nm^{-1}$ in the scattering profile of unmixed graphite powder corresponds to the d_{002} spacing of graphite ($d = 0.34$ nm).[64] A peak appears at the same q in the profile of PEN/graphite composites, which implies that graphite is still ordered in layers even after melt compounding. However, for neat FGS (Figure 5b), neither graphite nor graphite oxide ($q = 8.4-9.7\ nm^{-1}$, $d = 0.65-0.75$ nm)[63] peaks are present, signifying nearly complete exfoliation during the rapid thermal treatment. The characteristic reflections of graphite and graphite oxide is still absent after melt processing, corroborating the highly exfoliated morphology of FGS in PEN. There are no particular reflections for the stacked morphology of FGS planes observed by TEM

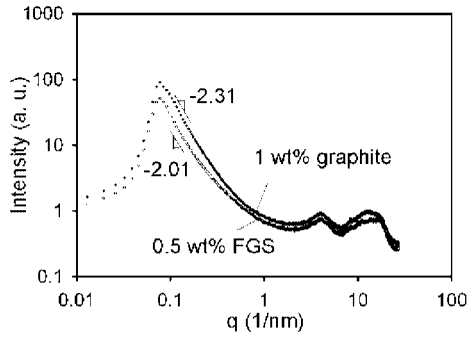

Figure 5. X-ray scattering profiles of 1 wt % graphite and 0.5 wt % FGS sample. Fractal dimensions of graphite and FGS were determined from the slope in the small angle range ($q = 0.13-0.25$ nm^{-1}). The beam block attenuated the intensity below $q = 0.1$ nm^{-1}.

(Figure 2d), which suggests that stacking is rare or that the sheets are more than 10 nm apart and thus scatter at lower angles than we can detect.

The slope of X-ray scattering intensity at small angles can give the dimension d_f of fractal aggregates.[44,65]

$$I(q) \propto \frac{1}{q^{d_f}} \tag{1}$$

Lower fractal dimension translates to a more open structure and thus higher level of dispersion. Figure 5 shows log scattering intensity vs log q for dilute FGS and graphite composites. The fractal dimensions averaged over the lowest accessible q range, $0.13-0.25$ nm^{-1} are 2.31 and 2.01, respectively. The aggregate structure at the length scale probed, ~10 nm, is less dense in FGS composites than in graphite composites.

3.4. Melt Rheology. Linear viscoelastic measurements were used to estimate fractal dimension and aspect ratio following the method developed by Vermant et al.[44] to study clay dispersion in polypropylene. The melt rheology results are summarized in Tables 1 and 2 along with the other composite properties.

3.4.1. Melt Stability of PEN Composites. Figure 6 shows the change in the elastic modulus G' at 1 rad/s vs annealing time at 290 °C. G' of the 2 wt % FGS composite displays about 40% growth with time and becomes constant by 2000 s. This increase in elastic constant may be due to rebuilding via Brownian motion of a network structure which was disrupted during sample loading. However, it may also arise from molecular weight increase of PEN. It was previously reported that molecular weight of polyesters, including PEN, in the melt state grows as annealing proceeds under an inert atmosphere via end-group reactions.[66] Since the samples were stored at 120 °C for at least 48 h before the testing, water content in PEN could be significantly reduced from its equilibrium value. Molecular weight will increase to the new equilibrium value by chain coupling.

3.4.2. Linear Viscoelastic Response. After performing the time sweep until no significant change (change less than 2% within 10 min) in G' was observed, strain sweep tests at 290 °C were subsequently carried out to find the limit of linear viscoelasticity. Figure 7 shows that the critical strain, γ_{crit} decreases significantly with filler content. The reduction at lower volume fraction originates from individual aggregates which enhance straining in the surrounding media.[44,67] The critical strain decreases more dramatically when it reaches a critical volume fraction for both types of fillers. For the graphite/PEN system, γ_{crit} of the 7 wt % sample is 100 times smaller than that of 3 wt %, whereas such a large change is not observed from 0 to 3 wt % (Figure 8). A similar drastic transition in the critical strain of FGS composites occurs near 1 wt % (0.5 vol %). Above this transition, γ_{crit} arises from the breakup of the connected network of FGS sheets reducing the elastic character of composite melts. At this higher volume fraction, critical strain tends to scale with a power of layered filler concentration.[44,47] The power law constant of this scaling is –3.07 for FGS and –1.24 for graphite (see Figure 8), indicating that the FGS network is much more strain sensitive.

Dynamic frequency sweep tests were conducted at $\gamma < \gamma_{crit}$. Storage moduli of PEN and PEN composites at 290 °C are shown in Figure 9 as a function of frequency. For the entire range of frequency, G' increases with concentration of graphite and FGS. Neat PEN and composites with low graphite incorporation display terminal behavior down to lowest test frequency (~0.01 rad/s). At higher concentration than 5 wt % for graphite and 1 wt % for FGS, G' shows a plateau at low frequency, which is a characteristic response of solidlike materials.[40,41] Interestingly, the critical volume fraction where transitions from terminal to nonterminal behavior take place coincides with the volume fraction where critical strain starts to decrease more sensitively with filler concentration. This coincidence implies that these two transitions stem from a common origin: formation of a space-filling elastic network. Above this particular volume fraction, there is a significant reinforcement in elastic moduli at low frequency, and this growth in moduli with the volume fraction of the additive is more pronounced with increasing the concentration of FGS than that of graphite. An increase in G' to ~ 10^5 GPa at 0.01 rad/s is achieved by adding only 4 wt % of FGS, but a same increase in G' requires 15−20 wt % of graphite.

3.4.3. Analysis Based on Percolation Concepts. The elasticity of layered composite melts signifies the presence of a space-filling rigid network which resists deformation. The elastic moduli of the percolated colloidal suspension can be expressed near the percolation threshold by a power law correlation on the difference between volume fraction of particles ϕ and the threshold value ϕ_{per}.[68–70]

$$G' \propto (\phi - \phi_{per})^{\nu} \tag{2}$$

Assuming the shear modulus of PEN dispersed with graphite and FGS follows this power law scaling, the percolation threshold ϕ_{per} and exponent ν of our system were evaluated by applying eq 2 to the G' value at $\omega = 0.1$ rad/s for graphite and at 0.01 rad/s for FGS composites. When converting weight fraction to volume fraction, densities provided in the Experimental Section were used ($\rho_{PEN} = 1.20$ and $\rho_{graphite} = 2.28$ g/cm^3). Least-squares regressions were carried out until optimum ϕ_{per} and ν were found that best fit the data. Figure 10 indicates that both systems exhibit a power law dependence. The onsets of percolation determined by using the power law relationship are 0.024 (4.8 wt %) and 0.0027 (0.51 wt %) for graphite and FGS, respectively. For FGS, the onset of percolation of 0.27 vol % is close to the point where the critical strain starts to drop more sensitively (0.47 vol %) from Figure 8. The scaling exponents of graphite and FGS systems are 2.16 and 3.78. The lower volume fraction at the onset of rigidity percolation and the higher exponent of FGS confirm that FGS is much more effective in increasing viscoelasticity of PEN. Theoretically, the power law exponent for the rigidity percolation of 3-dimensional networks is expected to be greater than 3.[70–72] Thus, FGS/PEN fits rigidity percolation, but for graphite/PEN melts the exponent is smaller than 3. As shown in the frequency sweep results of graphite composites, slow relaxation takes place as frequency becomes smaller than 0.1 rad/s at higher loading (7, 10, and 15 wt %). We chose G' at 0.1 rad/s for the analysis. Therefore, it is possible that the elastic character of PEN/graphite networks is not truly reflected by G' at 0.1 rad/s. Also, graphite with a low aspect ratio may form an unstable transient network in the

Table 1. Properties of PEN/Graphite Composites

concentration		rheology		surface resistance, D samples (B samples)	H_2 permeability	tensile modulus	
wt %	vol %[a]	γ_{crit} (%)	G' at 0.1 rad/s (Pa)	(ohms)	(barrers)	(GPa)	CTE $\times 10^5$ /°C
0	0	63	32.1	1.4×10^{13} (3.0×10^{12})	1.43	2.35	7.74
1	0.6	60	42.8			2.54	7.32
3	1.8	45	47.5		1.14	2.76	6.63
5	3.0	12	142	2.9×10^{12} (1.1×10^{12})	1.07	3.59	6.32
6	3.6			(1.4×10^{7})			
7	4.2	0.56	4310	1.5×10^{12} (1.1×10^{7})	0.90	4.02	5.48
10	6.1	0.34	22500	5.1×10^{10}	0.76	4.52	4.60
15	9.3	0.24	84200				
20	12.7	0.13	278000	(2.5×10^{5})		7.27	2.90

[a] Note that volume fraction of graphite shown here is based on the amorphous density of PEN (1.33 g/cm^3).

Table 2. Properties of PEN/FGS Composites

concentration		rheology		surface resistance, D samples	H_2 permeability	tensile modulus	
wt %	vol %[a]	γ_{crit} (%)	G' at 0.01 rad/s (Pa)	(ohms)	(barrers)	(GPa)	CTE $\times 10^5$ /°C
0.5	0.3	44	7.12	2.5×10^{13}			
1.0	0.6	43	98.7	1.3×10^{9}	1.05	2.70	7.22
1.5	0.8	9.1	943	7.1×10^{7}			
2.0	1.2	3.3	5870	1.1×10^{6}			
3.0	1.8	1.1	33100	2.1×10^{5}	0.94	3.09	6.77
4.0	2.4	0.4	185000	2.6×10^{4}	0.61	3.69	6.71

[a] Note that volume fraction of FGS shown here is based on the amorphous density of PEN (1.33 g/cm^3).

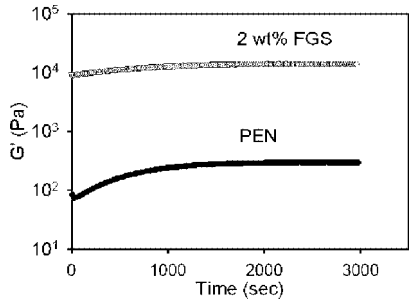

Figure 6. Evolution in G' at 1 rad/s for neat PEN and 2 wt % FGS at 290 °C with time after sample loading.

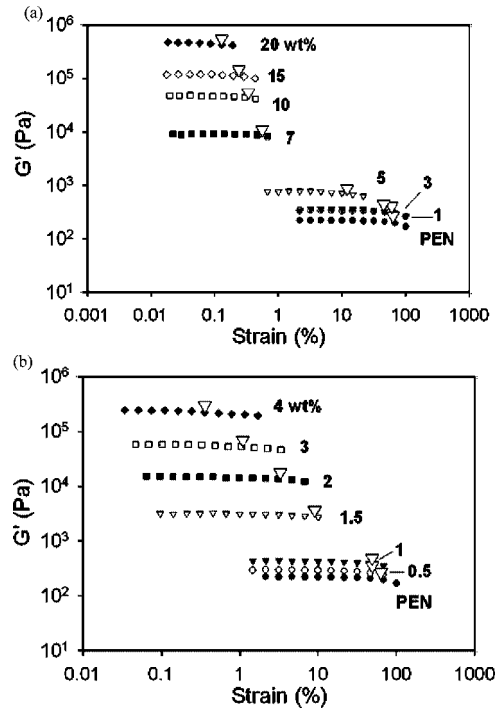

Figure 7. Dynamic strain sweeps of (a) graphite and (b) FGS composite melts at 290 °C. Critical strains, γ_{crit}, determined by $G'/G'_0 = 0.9$ are marked with ▽.

polymer host that does not transmit externally imposed load as efficiently as FGS.

The lower percolation threshold of FGS is strong evidence for better dispersion. Ren and co-workers showed that a relationship can be constructed between the percolation threshold and the aspect ratio, A_f, of a tactoid.[43] Supposing imaginary spheres surrounding each tactoid, the expression for the ratio of particle diameter $2r$ to thickness h can be written as

$$A_f = \frac{2r}{h} = \frac{3\phi_{sphere}}{2\phi_{per}} \quad (3)$$

Percolation of interpenetrating, randomly packed spheres occurs at $\phi_{sphere} = 0.29$.[73,74] Using the onsets of percolation of graphite and FGS from melt rheology (Table 3), eq 3 gives aspect ratios for graphite and FGS of 18 and 161, respectively (see Table 4). The average aspect ratio of FGS determined by rheological measurements is about 9 times higher than that of graphite, which is in line with TEM and X-ray scattering results.

3.4.4. Analysis Based on Fractal Gel Concepts. Our graphite/PEN system has many similarities with a flocculated suspension—high viscosity and nonzero elastic modulus[75–78]—and thus can be viewed as a colloidal gel. The scaling relationships between viscoelastic properties of colloidal gels and particle concentration proposed by Shih and co-workers[47] can be applied. Assuming the elastic network composed of graphite particles can be treated as fractal aggregates of graphite flocs, their shear moduli, G', and limits of linearity, γ_{crit}, above the gelation threshold can be scaled with the volume fraction of the flocs. When the bonds between flocs are stronger than the links within each floc

$$G' \propto \phi^{(3+x)/(3-d_f)} \quad (4)$$

$$\gamma_{crit} \propto \phi^{-(1+x)/(3-d_f)} \quad (5)$$

where d_f is the fractal dimension of the aggregates and x is the fractal dimension of the backbone in the aggregate which is

responsible for elasticity. In order to apply this model to our system, critical strains (Figure 7) and storage moduli at low frequency (Figure 9) above percolation threshold were chosen. As shown in Figures 8 and 11, G' and γ_{crit} scale with the filler volume fraction and more steeply with PEN/FGS than PEN/graphite. The G' scaling exponent of FGS composites is as high as 5.16, indicating the elastic network constructed with FGS is more efficient in storing elastic energy than that of graphite. The exponent of 5.16 for FGS composites is significantly higher than the scaling exponent reported for G' and the volume fraction of carbon nanotubes in polypropylene melts, ~2.8.[46] This large difference in scaling exponent implies that scaling behaviors depend on the dimensionality of reinforcing additives. Two-dimensional platelets should be more advantageous in enhancing elastic modulus than one-dimensional tubes.

Solving for d_f and x using eqs 4 and 5 gives $d_f = 2.04$ for FGS, which is close to the value obtained from X-ray scattering analysis ($d_f = 2.01$). The relatively high backbone fractal dimension $x = 1.95$ suggests that most elements in a FGS floc contribute to the elasticity of the network. In other words,

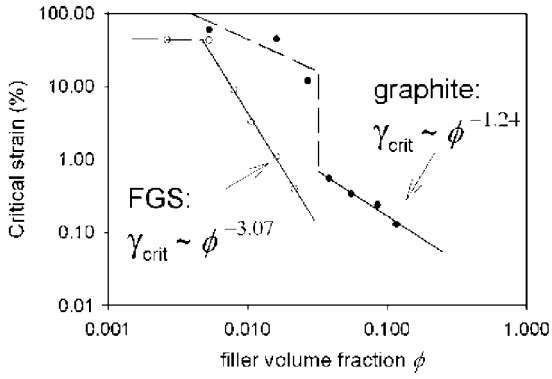

Figure 8. Scaling of critical strain at 1 rad/s of graphite (closed) and FGS (open symbols) composites melts.

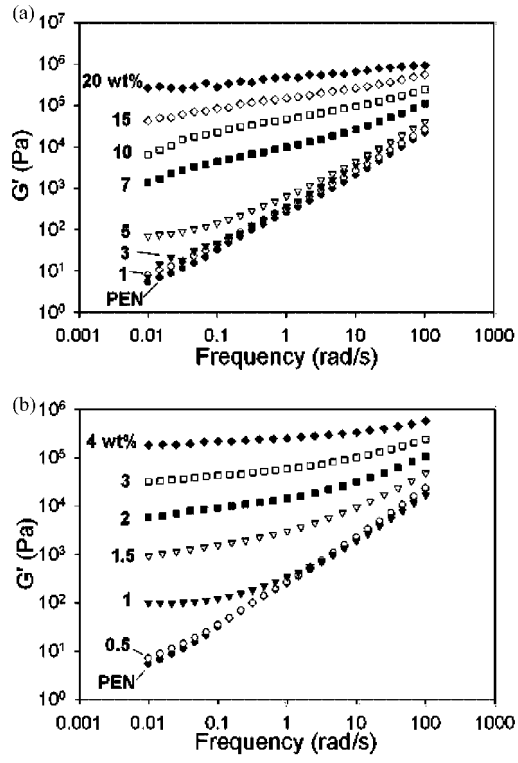

Figure 9. Dynamic frequency sweeps of (a) graphite and (b) FGS composite melts at 290 °C.

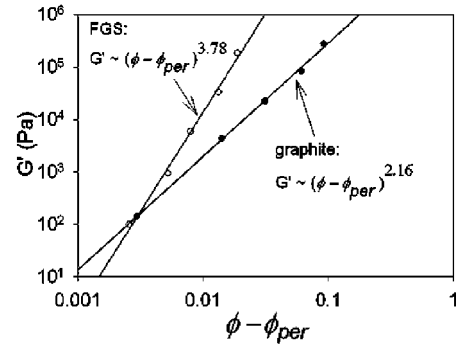

Figure 10. G' at $\omega = 0.1$ rad/s for graphite (closed) and 0.01 rad/s for FGS (open symbols) vs the difference between filler volume fraction and percolation volume fraction ($\phi_{perc} = 0.024$ for graphite and 0.0027 for FGS).

Table 3. Volumetric Percolation Threshold of Graphite and FGS Composites

	graphite/PEN	FGS/PEN
from melt rheology	0.024	0.0027
from electrical conductivity	0.030−0.036	0.003−0.006

Table 4. Comparisons of Aspect Ratios of Graphite and FGS from Different Characterization Techniques

	TEM	melt rheology	electrical conductivity	hydrogen permeability	tensile stiffness	thermal expansion
graphite	21	18	~13	16	21	16
FGS	88	161	~100	55	32[a]	10[a]

[a] Note that these aspect ratio values were obtained using in-plane tensile modulus and CTE of graphite.

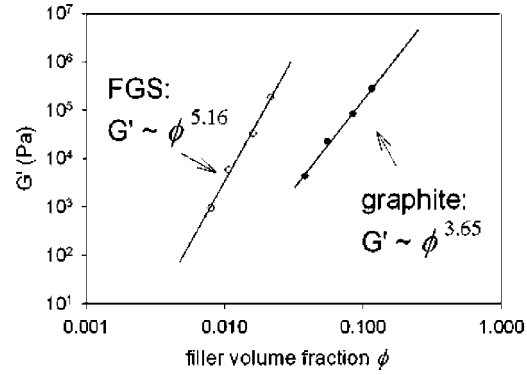

Figure 11. Scaling of G' at 0.1 rad/s for graphite (closed) and at 0.01 rad/s for FGS composites (open symbols) as a function of filler volume fraction.

structural defects which are elastically inactive such as dangling ends rarely exist. For the graphite system, Shih's model gives $d_f = 2.17$. However, the backbone fractal dimension of graphite flocs x is near 0, which is not physically realistic. This may reflect instability in the graphite/PEN network, which is also indicated by the decreasing low frequency G' values in Figure 9a.

3.5. Electrical Conductivity Measurements. Graphite is very attractive for its potential to increase the electrical conductivity of insulating polymers at very low concentration. Also, the threshold concentration for electrical conduction provides another measure of graphite dispersion. The connectivity percolation from conductivity measurements is valuable since it can be used to examine the validity of rigidity percolation data from melt rheology.

Similar to the viscoelastic properties, the electrical conductivity of composites reinforced with anisotropic conducting materi-

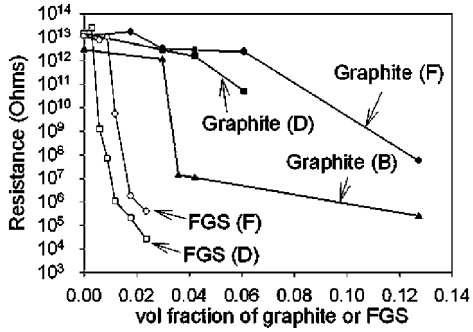

Figure 12. Surface resistance of graphite and FGS composites. D: ~1 mm thick disk-shaped samples after rheology tests with longer annealing history; F: ~70 μm thick biaxially squeezed film samples with filler orientation; B: bar-shaped samples (2 cm × 3 cm × 1 mm, molded from cryogenically pulverized powders and annealed 1 h at 300 °C).

als is easily influenced by the deformation history. It has been noted that rheological and electrical properties of suspensions of carbon nanotubes can be altered drastically by flow.[45,46] Surface resistance of composites produced under three different processing conditions (D, F, and B samples) are shown in Figure 12. At a certain concentration of graphitic reinforcements, resistance of PEN begins to drop precipitously. This transition indicates that graphite platelets provide connected pathways for electron transfer. The onset of electrical percolation clearly occurs at lower volume fraction for FGS, but there is an influence of the processing history in both. The thin, squeezed out, F samples exhibit a higher percolation threshold (graphite between 10 and 20 wt % and FGS between 1.5 and 2 wt %) than the thicker, annealed disk, D samples (graphite between 5 and 10 wt % and FGS between 0.5 and 1 wt %). The lower threshold of FGS can be explained by its higher aspect ratio. The higher threshold for F samples is attributed to the alignment of platelets parallel to the film surface during compression molding and loss in connectivity between platelets due to these alignments. In contrast, the lower percolation threshold for D samples owes to the structure recovery during rheology testing at elevated temperature. B samples which were formed by molding and then annealing cryo-pulverized powders exhibit the lowest percolation (between 5 and 6 wt %) among graphite samples. This process may create the most disordered state of graphite orientation and help graphitic disks to maintain their contact with other platelets. Annealing under the quiescent condition for longer times could lead to an even lower percolation threshold.

It is known that connectivity percolation takes place at a lower concentration of additives than rigidity percolation since networks that barely span the system volume may still have zero elasticity.[46,71,72,79] However, at least for our system, the threshold volume fractions for electrical percolation are comparable to or even higher than the rigidity percolation determined by rheological measurements (Table 3). For carbon nanotubes, Du and co-workers[45] showed that conductivity percolation was higher than rigidity percolation by rheology. They attribute this to polymer chains' bridging particles. In our case, the average diameter of the unperturbed PEN chains is ~16 nm,[80] which is greater than the distance for the electron tunneling to occur between graphite layers (~5 nm). Thus, bridging may account for the even lower onset of rigidity percolation from melt rheology than connectivity percolation. It is also possible that small deformation of the D samples during unloading from rheometer plates and remelting caused graphite layers to be oriented again, which in turn reduces connectivity between them. Also, the contact resistance between the sample and probes can interfere with measuring conductivity of samples, especially with low graphite loading.

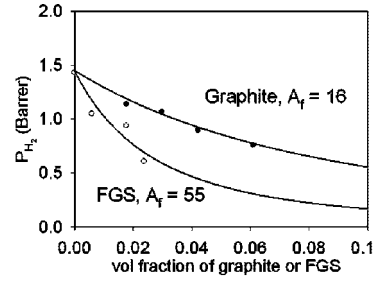

Figure 13. Hydrogen permeability of graphite (closed) and FGS (open symbols) composites at 35 °C. Curves represent theoretical trends based on Lape's model with A_f as an adjustable parameter.

3.6. Hydrogen Permeation. The high aspect ratio of graphitic additives suggests their potential use for reducing gas permeabilities of polymer films.[12,81] Gas permeability through a polymer filled with high aspect ratio, impermeable flakes can be decreased substantially via a reduced cross section for gas diffusion and a tortuous path mechanism.[82] After comparing several different models for gas permeability of membranes filled with aligned monodispersed impermeable disks, Picard et al.[39] found that the following model of Lape et al.[35] for flakes placed in random array describes the barrier performance of layered silicate nanocomposites most accurately:

$$\frac{P}{P_m} = \frac{1-\phi}{(1+A_f\phi/3)^2} \quad (6)$$

where P_m and P are permeabilities of gas molecules through unfilled and filled polymer membranes and ϕ is a volume fraction of disks. Since Lape's formula is a function of the aspect ratio, we can use it to evaluate dispersion. Hydrogen permeability at 35 °C through the 70 μm film samples (F samples) is shown in Figure 13 after converting filler weight fraction into volume fraction using the amorphous density of PEN (ρ_{PEN} = 1.33 and $\rho_{graphite}$ = 2.28 g/cm^3). Both graphite and FGS reduce the hydrogen permeability of PEN. Fitting these data with Lape's model gives a higher aspect ratio for FGS (A_f = 55) than graphite (A_f = 16). The aspect ratio for FGS inferred is lower than one from TEM, $A_f \sim 88$, rheological measurements, $A_f \sim 161$, or electrical conductivity, $A_f \sim 100$ (Table 4). The barrier performance may be reduced by the defect vacancies in FGS sheets, produced by the superheating synthesis process (i.e., holes on the FGS surface).[28] Also, graphitic flakes are not perfectly aligned in the plane of the film, contrary to the assumption of the composite theory.

3.7. Mechanical Properties. The exceptionally high stiffness and aspect ratio gives graphite potential for enhancing mechanical properties of polymers.[11] Tensile modulus and thermal expansion of PEN/graphite and PEN/FGS composites were measured and compared to composite theories (see Tables 1 and 2).

3.7.1. Tensile Modulus. Embedding materials with high stiffness into polymers leads to an increase in material stiffness allowing for stress redistribution from a low modulus matrix to a high modulus filler phase.[83] Complex Young's moduli of composites from strain sweep tests are presented in Figure 14. While there were significant improvements in stiffness of the composite from incorporating graphitic reinforcements, FGS turns out to be only slightly better than graphite in improving stiffness. For instance, the tensile modulus of 4 wt % (ϕ_{FGS} = 0.024) PEN/FGS composites is 3.7 GPa vs 3.6 GPa for PEN containing 5 wt % graphite ($\phi_{graphite}$ = 0.030).

The dispersion of layered nanocomposites was analyzed quantitatively using micromechanical models for composite stiffness.[36,38] Mori and Tanaka showed that moduli of com-

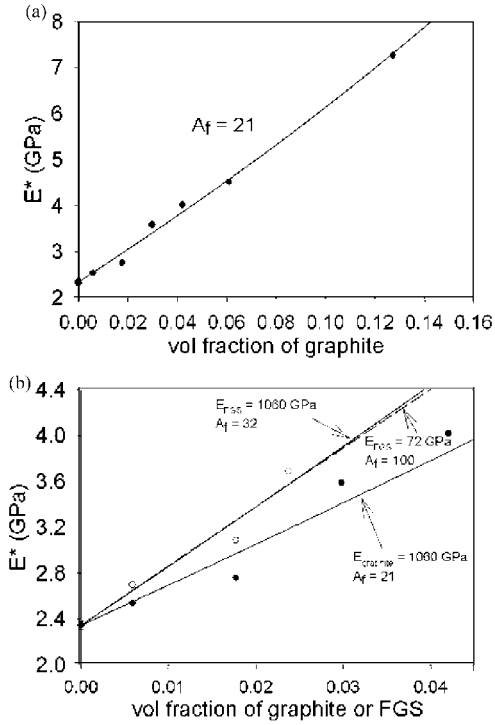

Figure 14. (a) Tensile moduli of graphite. (b) Moduli of graphite (closed) and FGS (open symbols) composites are compared at low filler concentration. Straight lines are predictions based on Mori−Tanaka theory. A dashed line shows how theoretical stiffness changes when in-plane tensile modulus and aspect ratio of FGS are changed to 72 GPa and 100, respectively.

posites filled with unidirectionally aligned ellipsoids can be predicted when the stiffness and the Poisson's ratio of each component and the aspect ratio of reinforcement are known.[32] Tandon and Weng adopted these ideas to derive analytical expressions for effective elastic moduli of composites which are transverse isotropic.[33] Their prediction for the transverse Young's modulus E_{11} is

$$\frac{E_{11}}{E_m} = \frac{1}{1+\phi(-2\nu_m A_3 + (1-\nu_m)A_4 + (1+\nu_m)A_5 A)/2A} \quad (7)$$

E_m and ν_m are Young modulus and Poisson's ratio of the matrix, respectively. A and A_i are functions of ϕ, ν_m, the Eshelby tensor,[84,85] Young's modulus of the matrix and the filler, and the filler aspect ratio. Exact formulas are provided by Tandon and Weng.[33] Using material data provided in the Appendix, the aspect ratio was determined that best fit experimental results. The aspect ratio of graphite and FGS based on this analysis is 21 and 32, respectively.

While a higher degree of exfoliation for FGS is in agreement with results from other characterization techniques, an aspect ratio of 32 for FGS is much smaller than ones from rheology and conductivity measurements. It should be noted that for this analysis in-plane modulus of a single graphene sheet was assumed to be 1060 GPa, which may not be valid for FGS which have structural abnormalities (wrinkling and atomistic defects) that the stiffness modeling cannot account for. For the case of carbon nanotubes, the waviness of flexible additives is reported to significantly reduce the overall stiffness of their composites with polymers.[86] Also, the wrinkled structure of FGS will precipitously reduce the elastic modulus in tensile deformation since a main deformation mode under the extension will be bending of the crumpled sheets rather than stretching of or bending between sp^2-hybridized C−C bonds. If we assume the aspect ratio of FGS evaluated from conductivity measurements

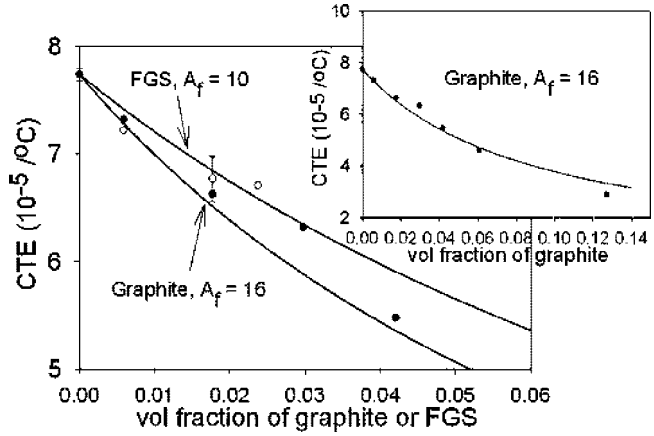

Figure 15. Coefficients of thermal expansion of graphite (closed) and FGS (open symbols) composites. Solid curves are model predictions based on Chow's theory with A_f as an adjustable parameter. The inset shows thermal expansion of graphite composites at higher graphite concentration.

is true ($A_f \sim 100$), from the Mori−Tanaka model the same extent of stiffening will be achieved when effective in-plane stiffness of FGS sheets is around 72 GPa (see Figure 14b). Further study to determine the effective tensile stiffness of FGS will be required to obtain more accurate measures for the aspect ratio of these two-dimensional thin sheets.

3.7.2. Thermal Expansion. Another advantage that can be expected from dispersing high aspect ratio rigid platelets with superior dimensional stability is a reduction in thermal expansion of polymeric materials.[12,87] Internal stress from a thermal expansion mismatch between two phases is transmitted across an interface, minimizing the overall dimensional change of matrix material.[83] Thermal expansion coefficients are shown in Figure 15 and Tables 1 and 2. The thermal expansion of PEN was suppressed by nearly the same amount, ~15%, by incorporating 3 wt % of graphite or FGS. The performance of FGS is surprisingly poor considering its high aspect ratio and the negative in-plane thermal expansion of graphite. The aspect ratio of both platelike additives can be estimated on the basis of a model proposed by Chow.[34,37] He used Eshelby's misfit theory[84,85] to derive theoretical predictions for coefficients of thermal expansion (CTE) of a polymer filled with aligned ellipsoids. The effective transverse CTE, α_{11}, is

$$\alpha_{11} = \alpha_m + \frac{K_f}{K_m}\frac{(\beta_f - \beta_m)J_3\phi}{2I_1J_3 + J_1I_3} \quad (8)$$

β_i and K_i are the volumetric thermal expansion coefficient and the bulk modulus of filler f or matrix m, respectively. I_j and J_j ($j = 1$ or 3) are functions of β_i, K_i, shear moduli G_i of each component, volume fraction of filler ϕ, and elements of Eshelby's tensor. Exact formulas are found in ref 34. Regression with experimental data using material parameters provided in the Appendix suggests that the aspect ratios of graphite and FGS are 16 and 10, respectively. Theoretical modeling based on Chow's theory suggests that FGS only provides retraction in thermal expansion that is comparable with what rigid disks ($E = 1060$ GPa and $\alpha_{||} = -1.5 \times 10^{-6}$/°C) with aspect ratio of 10 potentially do. This low reinforcement efficiency of FGS is again probably due to the highly distorted and wavy structure of FGS which may render FGS less resistive to tensile deformation and thermal expansion than rigid graphite platelets. Moreover, it must be noted that the theory assumes perfect interfacial adhesion between the matrix and filler and unidirectional alignment of platelets.

4. Conclusions

FGS, a thermally exfoliated graphite oxide, and graphite were melt blended into PEN using a small scale, twin-screw extruder. Electron microscopy and X-ray scattering techniques were employed to investigate dispersion of graphite and FGS directly. Both methods demonstrated that FGS sheets form an exfoliated morphology ($A_f = 88$) in the PEN matrix after melt compounding, whereas graphite is incorporated as unintercalated thick tactoids ($A_f = 21$). Melt rheology was also used to probe the microstructure of graphite and FGS in a PEN melt. Both graphite and FGS show linear viscoelastic behavior characterized by a reduction in critical strain and an increase in low-frequency shear modulus as the concentration of the reinforcement is increased. The extent of dispersion of both fillers was determined quantitatively from the critical percolation volume fraction. The aspect ratio of FGS ($A_f = 161$) from rheological measurements is substantially higher than that of graphite ($A_f = 18$), which agrees with TEM estimates. It is also consistent with the higher fractal dimension of graphite ($d_f = 2.31$) than FGS ($d_f = 2.01$) from X-ray scattering.

Electrical percolation data compared favorably with the threshold for rigidity percolation from rheological measurements for both fillers. A significantly lower electrical percolation threshold with FGS ($\phi_{per} \sim 0.003$) compared with graphite ($\phi_{per} \sim 0.030$) also confirmed better dispersion of FGS sheets. When we compare these with other systems, the onsets of rigidity and connectivity percolation for FGS are as low as those reported for carbon nanotube networks, $\phi_{per} \sim 0.003$.[45,46] Gas barrier performance of composites reinforced with FGS was superior to that of graphite composites, and this was attributed to its higher aspect ratio. However, stiffness and dimensional stability gained by incorporating FGS are not as notable as the improvements of other properties. We believe that this is due to atomistic defects from oxidation and pyrolysis and also from wrinkling of FGS sheets. These structural characteristics could reduce the effective tensile stiffness and thus reinforcement efficiency of FGS, in spite of its high aspect ratio. If graphite can be exfoliated and maintain its structural flatness and rigidity after the exfoliation, mechanical and thermal properties may be enhanced. However, the wrinkled structure of FGS may be valuable in reducing reaggregation.

In summary, all the estimations for the dispersion of graphite platelets from characterization based on different physical phenomena agree quantitatively ($A_f = 13-21$) while aspect ratios of FGS spread over a wide range (Table 4). As mentioned earlier, using the same in-plane stiffness and CTE for both graphite and FGS is problematic. Another reason for this large discrepancy among A_f values for FGS could be complexities associated with real composite morphology, such as imperfect interfacial bonding, random orientation, and size distribution of anisotropic fillers, that composite theories used in this study do not account for. Attempts to take these departures from ideality into account should be made to obtain more reliable measures for the dispersion of layered nanocomposites.

Acknowledgment. The authors acknowledge financial support from the NIST ATRP program with IMATION Corp. and the University of Minnesota Industrial Partnership for Research in Interfacial and Materials Engineering (IPRIME) and General Motors Corp. We also thank Prof. Ilhan Aksay, Prof. Robert Prud'homme at Princeton University, and John Lettow of Vorbeck Materials for providing the FGS, Michael Beaulieu for help with melt blending, Prof. Michael Tsapatsis at the University of Minnesota for use of the gas permeation apparatus, Rich Hoffman at Entegris for his help with electrical conductivity measurements, and Dr. Kwanho Chang of the University of Minnesota for his help with TEM operation.

Appendix. Material Parameters Used for Composite Modeling

The experimentally measured Young's modulus of PEN ($E_{PEN} = 2.35$ GPa) and the literature modulus of graphite in the basal plane ($E_{graphite} = 1060$ GPa)[5] were used for composite modeling based on Mori−Tanaka and Chow's model. Poisson's ratios ν of PEN and graphite are 0.32[88] and 0.006.[89] As pointed out by Cho et al.,[89] out-of-plane Poisson's ratio values of graphite determined either experimentally or theoretically vary over a wide range. However, whichever value is chosen for this analysis, there is no significant variation in predicted aspect ratio since the effect of Poisson deformation is negligible due to the small thickness of the platelets. For PEN films, coefficients of thermal expansion in plane, $\alpha_{PEN||}$, and in thickness direction, $\alpha_{PEN\perp}$, are estimated to be 7.74×10^{-5} and 8.55×10^{-5}/°C, respectively, from measurements with a Rheometrics Solids Analyzer and a Dynamic Mechanical Analyzer 7E (Perkin-Elmer). It is assumed that $\alpha_{||}$ and $\alpha_{\perp}$ are -1.5×10^{-6}/°C and 27×10^{-6}/°C for both graphite and FGS.[49,50] Summation of linear CTE's in three perpendicular directions ($\beta = 2\alpha_{||} + \alpha_{\perp}$ for transversely isotropic materials) gave the volumetric coefficients of thermal expansion, β, of 2.4×10^{-4} for PEN and 2.4×10^{-5}/°C for graphite and FGS. By approximating matrix and filler phase as isotropic, $K_{PEN} = E_{PEN}/2(1 + \nu_{PEN}) = 0.89$ GPa, $K_{graphite} = 527$ GPa, $G_{PEN} = E_{PEN}/(3 - 2\nu_{PEN}) = 2.17$ GPa, and $G_{graphite} = 358$ GPa.[83]

References and Notes

(1) Tamashuasky, A. V. In National Lubricating Grease Institute 72nd Annual Meeting, San Antonio, TX, 2005.
(2) Chung, D. D. L. *J. Mater. Sci.* **1987**, *22*, 4190.
(3) Drzal, L. T.; Fukushima, H. *Polym. Prepr. (Am. Chem. Soc., Div. Polym. Chem.* **2001**, *42*, 42.
(4) Fukushima, H.; Drzal, L. T. *Annu. Tech. Conf.—Soc. Plast. Eng.* **2003**, 2230.
(5) Kelly, B. T. *Physics of Graphite*; Applied Science: London, 1981.
(6) Schadler, L. S.; Giannaris, S. C.; Ajayan, P. M. *Appl. Phys. Lett.* **1998**, *73*, 3842.
(7) Novoselov, K. S.; Geim, A. K.; Morozov, S. V.; Jiang, D.; Zhang, Y.; Dubonos, S. V.; Grigorieva, I. V.; Firsov, A. A. *Science* **2004**, *306*, 666.
(8) Zhang, Y.; Tan, Y.-W.; Stormer, H. L.; Kim, P. *Nature (London)* **2005**, *438*, 201.
(9) Tsuzuku, T. *Carbon* **1979**, *17*, 293.
(10) Smith, A. W.; Rasor, N. S. *Phys. Rev.* **1956**, *104*, 885.
(11) Kalaitzidou, K.; Fukushima, H.; Drzal, L. T. *Composites: Part A* **2007**, *38*, 1675.
(12) Kalaitzidou, K.; Fukushima, H.; Drzal, L. T. *Carbon* **2007**, *45*, 1446.
(13) Viculis, L. M.; Mack, J. J.; Mayer, O. M.; Hahn, H. T.; Kaner, R. B. *J. Mater. Chem.* **2005**, *15*, 974.
(14) Carr, K. E. *Carbon* **1970**, *8*, 155.
(15) Chen, G.; Wu, D.; Weng, W.; Wu, C. *Carbon* **2003**, *41*, 619.
(16) Zheng, W.; Wong, S.-C.; Sue, H.-J. *Polymer* **2002**, *43*, 6767.
(17) Zou, J.-F.; Yu, Z.-Z.; Pan, Y.-X.; Fang, X.-P.; Ou, Y.-C. *J. Polym. Sci., Part B: Polym. Phys.* **2002**, *40*, 954.
(18) Pan, Y.-X.; Yu, Z.-Z.; Ou, Y.-C.; Hu, G.-H. *J. Polym. Sci., Part B: Polym. Phys.* **2000**, *38*, 1626.
(19) Fukushima, H. Ph.D. Thesis, Michigan State University, **2003**.
(20) Kalaitzidou, K.; Fukushima, H.; Drzal, L. T. *Compos. Sci. Technol.* **2007**, *67*, 2045.
(21) Shen, J.-W.; Chen, X.-M.; Huang, W.-Y. *J. Appl. Polym. Sci.* **2003**, *88*, 1864.
(22) Liu, L.; Qi, Z.; Zhu, X. *J. Appl. Polym. Sci.* **1999**, *71*, 1133.
(23) Dennis, H. R.; Hunter, D. L.; Chang, D.; Kim, S.; White, J. L.; Cho, J. W.; Paul, D. R. *Polymer* **2001**, *42*, 9513.
(24) Lincoln, V. F.; Claude, Z. US Patent 4,414,142, **1983**.
(25) Zheng, W.; Lu, X.; Wong, S.-C. *J. Appl. Polym. Sci.* **2004**, *91*, 2781.
(26) Schniepp, H. C.; Li, J.-L.; McAllister, M. J.; Sai, H.; Herrera-Alonso, M.; Adamson, D. H.; Prud'homme, R. K.; Car, R.; Saville, D. A.; Aksay, I. A. *J. Phys. Chem. B* **2006**, *110*, 8535.
(27) Prud'homme, R. K.; Aksay, I. A.; Adamson, D. H.; Abdala, A. US Patent 20070092432 A1, **2007**.
(28) Li, J.-L.; Kudin, K. N.; McAllister, M. J.; Prud'homme, R. K.; Aksay, I. A.; Car, R. *Phys. Rev. Lett.* **2006**, *96*, 176101/1.
(29) Vaia, R. A.; Jandt, K. D.; Kramer, E. J.; Giannelis, E. P. *Macromolecules* **1995**, *28*, 8080.

(30) Lee, H.-S.; Fasulo, P. D.; Rodgers, W. R.; Paul, D. R. *Polymer* **2005**, *46*, 11673.
(31) Vaia, R. A.; Jandt, K. D.; Kramer, E. J.; Giannelis, E. P. *Chem. Mater.* **1996**, *8*, 2628.
(32) Mori, T.; Tanaka, K. *Acta Metall.* **1973**, *21*, 571.
(33) Tandon, G. P.; Weng, G. J. *Polym. Compos.* **1984**, *5*, 327.
(34) Chow, T. S. *J. Polym. Sci., Part B: Polym. Phys.* **1978**, *16*, 967.
(35) Lape, N. K.; Nuxoll, E. E.; Cussler, E. L. *J. Membr. Sci.* **2004**, *236*, 29.
(36) Fornes, T. D.; Paul, D. R. *Polymer* **2003**, *44*, 4993.
(37) Yoon, P. J.; Fornes, T. D.; Paul, D. R. *Polymer* **2002**, *43*, 6727.
(38) Sheng, N.; Boyce, M. C.; Parks, D. M.; Rutledge, G. C.; Abes, J. I.; Cohen, R. E. *Polymer* **2004**, *45*, 487.
(39) Picard, E.; Vermogen, A.; Gerard, J. F.; Espuche, E. *J. Membr. Sci.* **2007**, *292*, 133.
(40) Krishnamoorti, R.; Giannelis, E. P. *Macromolecules* **1997**, *30*, 4097.
(41) Solomon, M. J.; Almusallam, A. S.; Seefeldt, K. F.; Somwangthanaroj, A.; Varadan, P. *Macromolecules* **2001**, *34*, 1864.
(42) Jeon, H. S.; Rameshwaram, J. K.; Kim, G. *J. Polym. Sci., Part B: Polym. Phys.* **2004**, *42*, 1000.
(43) Ren, J.; Silva, A. S.; Krishnamoorti, R. *Macromolecules* **2000**, *33*, 3739.
(44) Vermant, J.; Ceccia, S.; Dolgovskij, M. K.; Maffettone, P. L.; Macosko, C. W. *J. Rheol.* **2007**, *51*, 429.
(45) Du, F.; Scogna, R. C.; Zhou, W.; Brand, S.; Fischer, J. E.; Winey, K. I. *Macromolecules* **2004**, *37*, 9048.
(46) Kharchenko, S. B.; Douglas, J. F.; Obrzut, J.; Grulke, E. A.; Migler, K. B. *Nat. Mater.* **2004**, *3*, 564.
(47) Shih, W. H.; Shih, W. Y.; Kim, S. I.; Liu, J.; Aksay, I. A. *Phys. Rev. A* **1990**, *42*, 4772.
(48) Weick, B. L.; Bhushan, B. *IEEE Trans. Magn.* **1995**, *31*, 2937.
(49) Nelson, J. B.; Riley, D. P. *Proc. Phys. Soc.* **1945**, *57*, 477.
(50) Kelly, B. T. *Carbon* **1972**, *10*, 429.
(51) www.asbury.com, accessed Sept 15, **2007**.
(52) www.vorbeck.com, accessed Sept 15, **2007**.
(53) Ouchi, I.; Aoki, H.; Shimotsuma, S.; Asai, T.; Hosoi, M. *Proc. Jpn. Congr. Mater. Res.* **1974**, *17*, 217.
(54) Mencik, Z. *Chem. Prum.* **1967**, *17*, 78.
(55) Buchner, S.; Wiswe, D.; Zachmann, H. G. *Polymer* **1989**, *30*, 480.
(56) Daubeny, R. d. P.; Bunn, C. W.; Brown, C. J. *Proc. R. Soc. London* **1954**, *A226*, 531.
(57) http://www.stelray.com/density_val.htm, accessed Sep 15, **2007**.
(58) Pye, D. G.; Hoehn, H. H.; Panar, M. *J. Appl. Polym. Sci.* **1976**, *20*, 1921.
(59) Jeong, H.-K.; Krych, W.; Ramanan, H.; Nair, S.; Marand, E.; Tsapatsis, M. *Chem. Mater.* **2004**, *16*, 3838.
(60) The specific surface area (A) from BET isotherm can be related to the density and the thickness (h) of the disks assuming the area of the disk at the perimeter is negligible. $h \approx 2/A \cdot$(density).
(61) Kudin, K. N.; Ozbas, B.; Schniepp, H. C.; Prud'homme, R. K.; Aksay, I. A.; Car, R. *Nano Lett.* **2008**, *8*, 36.
(62) Dresselhaus, M. S.; Dresselhaus, G.; Jorio, A.; Souza Filho, A. G.; Saito, R. *Carbon* **2002**, *40*, 2043.
(63) Hontoria-Lucas, C.; Lopez-Peinado, A. J.; Loepz-Gonzalez, J. d. D.; Rojas-Cervantes, M. L.; Martin-Aranda, R. M. *Carbon* **1995**, *33*, 1585.
(64) Bacon, G. E. *Acta Crystallogr.* **1951**, *4*, 558.
(65) Schaefer, D. W.; Justice, R. S.; Koerner, H.; Vaia, R.; Zhao, C.; Yang, M.; Vale, J. *Mater. Res. Soc. Symp. Proc.* **2005**, *840*, 57.
(66) Yoon, K. H.; Lee, S. C.; Park, I. H.; Lee, H. M.; Park, O. O.; Son, T. W. *Polymer* **1997**, *38*, 6079.
(67) Ohl, N.; Gleissle, W. *J. Rheol.* **1993**, *37*, 381.
(68) Zosel, A. *Rheol. Acta* **1982**, *21*, 72.
(69) Wong, R. B. K.; Lelievre, J. *Rheol. Acta* **1981**, *20*, 299.
(70) Kanai, H.; Navarrete, R. C.; Macosko, C. W.; Scriven, L. E. *Rheol. Acta* **1992**, *31*, 333.
(71) Feng, S.; Sen, P. N. *Phys. Rev. Lett.* **1984**, *52*, 216.
(72) Thorpe, M. F. In *Physics of Disordered Materials*; Adler, D., Fritzsche, H., Ovshinsky, S., Eds.; Plenum Press: New York, 1985; p 55.
(73) Shante, V. K. S.; Kirkpatrick, S. *Adv. Phys.* **1971**, *20*, 325.
(74) Balberg, I. *Phys. Rev. B* **1985**, *31*, 4053.
(75) Patel, P. D.; Russel, W. B. *J. Rheol.* **1987**, *31*, 599.
(76) Heyes, D. M.; McKenzie, D. J.; Buscall, R. *J. Colloid Interface Sci.* **1991**, *142*, 303.
(77) Rueb, C. J.; Zukoski, C. F. *J. Rheol.* **1997**, *41*, 197.
(78) Rueb, C. J.; Zukoski, C. F. *J. Rheol.* **1998**, *42*, 1451.
(79) Head, D. A.; Levine, A. J.; MacKintosh, F. C. *Phys. Rev. E* **2003**, *68*, 061907/1.
(80) Since Mark−Houwink parameters for PEN in *o*-chlorophenol are not available, viscosity-average molecular weight, M_v, of PEN is estimated to be 72 000 g/mol from the intrinsic viscosity (0.79 dL/g) using values for poly(ethylene terephthalate) in the same solvent ($k = 2.25 \times 10^{-4}$ dL/g and $a = 0.73$; Hergenrother, W. L.; Nelson, C. J. *J. Polym. Sci., Part A: Polym. Chem.* **1974**, *12*, 2905). Assuming weight-average molecular weight can be approximated by M_v and the polydispersity index is ~2, which is typical for condensation polymers, gives number-average molecular weight of 36 000 g/mol and average degree of polymerization of ~148. The theoretically estimated characteristic ratio ($C_r = \langle r^2\rangle_0/(n\langle l^2\rangle)$ of unperturbed PEN chains is 5.39 (Tonelli, A. E. *Polymer* **2001**, *43*, 637) and the length of PEN repeating unit, l, is 0.68 nm using group additivity. Thus, the average diameter of the random PEN coil (twice of radius of gyration, $2(\langle r^2\rangle_0/6)^{0.5}$) is ~16 nm.
(81) Matayabas, J. C., Jr.; Turner, S. R. In *Polymer-Clay Nanocomposites*; Pinnavaia, T. J., Beall, G. W., Eds.; John Wiley & Sons: Chichester, 2000.
(82) Cussler, E. L.; Hughes, S. E.; Ward, W. J., III; Aris, R. *J. Membr. Sci.* **1988**, *38*, 161.
(83) Hull, D.; Clyne, T. W. *An Introduction to Composite Materials*, 2nd ed.; Cambridge University Press: London, 1996.
(84) Eshelby, J. D. *Proc. R. Soc. London* **1957**, *241*, 376.
(85) Eshelby, J. D. *Proc. R. Soc. London* **1959**, *252*, 561.
(86) Fisher, F. T.; Bradshaw, R. D.; Brinson, L. C. *Compos. Sci. Technol.* **2003**, *63*, 1689.
(87) Yano, K.; Usuki, A.; Okada, A. *J. Polym. Sci., Part A: Polym. Chem.* **1997**, *35*, 2289.
(88) Ma, T.; Bhushan, B.; Murooka, H.; Kobayashi, I.; Osawa, T. *Rev. Sci. Instrum.* **2002**, *73*, 1813.
(89) Cho, J.; Luo, J. J.; Daniel, I. M. *Compos. Sci. Technol.* **2007**, *67*, 2399.

MA702385H